Appl Biochem Biotechnol
DOI 10.1007/s12010-017-2443-2

Evaluation of Magnetonanoparticles Conjugated with New Angiogenesis Peptides in Intracranial Glioma Tumors by MRI

Erica Aparecida de Oliveira[1,2] · Jelena Lazovic[3] · Lea Guo[3] · Horacio Soto[4] · Bluma Linkowski Faintuch[1] · Massoud Akhtari[5] · Whitney Pope[3]

Received: 10 January 2017 / Accepted: 20 February 2017

Abstract Angiogenesis plays a critical role in progression of malignant gliomas. The development of glioma-specific labeling molecules that can aid detection and visualization of angiogenesis can help surgical planning and improve treatment outcome. The aim of this study was to evaluate if two peptides (GX1 and RGD-GX1) linked to angiogenesis can be used as an MR-imaging markers of angiogenesis. MR imaging was performed in U87 glioblastoma-bearing NOD-SCID mice at different time points between 15 and 120 min post-injection to visualize particle distribution. GX1 and RGD-GX1 exhibited the highest accumulation in U87 glioblastoma at 120 min post i.v. administration. GX1-conjugated agents lead to higher decrease in transverse relaxation time (T_2) (i.e., stronger contrast enhancement) than RGD-GX1-conjugated agents in U87 glioblastoma tumor model. In addition, we tested if U87-IDH1^{R132} mutated cell line had different pattern of GX1 or RGD-GX1 particle accumulation. Responses in U87-IDH1^{WT} followed a similar pattern with GX1 contrast agents; however, lower contrast enhancement was observed with RGD-GX1 agents. The specific

✉ Erica Aparecida de Oliveira
ericaoliveira@usp.br

[1] Radiopharmacy Center, Institute of Energy and Nuclear Research, Av. Prof. Lineu Prestes 2242, São Paulo, SP 05508-000, Brazil

[2] Present address: School of Pharmaceutical Sciences, University of Sao Paulo, Av. Prof. Lineu Prestes, 580 Bloco 17, São Paulo, SP 05508-900, Brazil

[3] Department of Radiology, David Geffen School of Medicine, University of California, Los Angeles, CA, USA

[4] Department of Neurosurgery, David Geffen School of Medicine, University of California, Los Angeles, CA, USA

[5] Jane and Terry Semel Institute for Neuroscience and Human Behavior, David Geffen school of Medicine, University of California, Los Angeles, CA, USA

Published online: 09 March 2017

binding of these peptides to human glioblastoma xenograft in the brain was confirmed by magnetic resonance imaging. The contrast enhancement following injection of magnetonanoparticles conjugated to GX1 peptide matched well with CD31 staining and iron staining.

Keywords GX1 peptide · RGD-GX1 peptide · Angiogenesis · MRI · Glioma

Introduction

Gliomas, and particularly glioblastoma multiforme, are the most frequent primary brain tumors with high malignancy and poor prognosis in adults, with an incidence estimated to be 3–5/100,000 per year. The average survival of patients with glioblastoma multiforme is 35% after 1 year and less than 5% at 5 years [1].

Angiogenesis plays a critical role in glioma development and growth, even during the earliest phases. It is also permissive for metastasis and represents a pathological hallmark of cancer. The level of angiogenesis correlates with the aggressiveness of gliomas and is often associated with prognosis [2, 3].

Genomic analysis of human glioblastoma multiforme (GBM) reveals a mutation in the active site of isocitrate dehydrogenase–1 (IDH1) in 12% of GBM patients [4]. The mutation affecting arginine at residue 132 (R132) of the IDH1 protein ($IDH1^{R132}$) has been identified in >70% of lower-grade gliomas [5]. The R132 residue is conserved among species, probably representing the substrate-binding site [6]. $IDH1^{R132}$ seems to be an early event in gliomagenesis and might contribute to malignant transformation [7].

By means of in vivo screening of a phage-display peptide library, the affinity of the RGD and the GX1 peptides for angiogenesis has previously been recognized [8, 9]. The RGD motif is well studied, being known for its binding specificity to $\alpha v\beta 3$ integrin receptors, which are present in angiogenesis and also in glioma [10–14]. RGD peptide is involved in many processes important to tumor progression, such as cell attachment and spreading, attracting attention for cancer targeting approaches [15–19].

GX1(CGNSNPKSC) is a novel peptide in this setting, already studied as vascular marker for human cancers with some protocols suggesting application to tumor targeting and imaging, although there is still a lack in the understanding the mechanism of GX1 [20–24].

The RGD peptide has been combined with other peptides, creating heterodimers such as Bombesin-RGD and RGD-αMSH (melanocyte-stimulating hormone), thereby aiming to improve tumor cell affinity by means of binding to two different kinds of receptors [25–28]. The dual-targeting approach has been addressed in many studies with successful results as described in Liu and Wang [29] review.

Preliminary studies showed the radiolabeling of these sequences with technetium-99m [30]. Also, these peptides were radiolabeled and evaluated in a glioma model indicating binding superiority to the RGD-GX1 peptide [31]. All these studies indicate that these peptides hold promise both for targeting and anti-angiogenic therapies.

In this study, the aim was evaluation of in vivo binding properties of the GX1 peptide alone and also the heterodimer RGD-GX1, both conjugated with magnetonanoparticles, by means of magnetic resonance imaging (MRI). We hypothesized that the strength of MRI contrast enhancement due to these contrast agents was associated with the level of tumor vascularization and that a

heterodimer probe would increase the affinity for new vessels. This study was envisioned as proof of concept, and future studies will be performed to confirm the findings.

Methods

Cell Lines

Tumor cell line of human glioblastoma U87MG and its clones overexpressing $IDH1^{WT}$ and $IDH1^{R132}$ protein were used. All cells were grown in Dulbecco's modified Eagle medium and Ham's F12 nutrient mixture (DMEM/F12), supplemented with 10% fetal bovine serum (FBS), 2 mM glutamine, and 100 u/mL of penicillin/streptomycin. Cells were kept in a 90% humidified tissue incubator containing 5% CO_2 at 37 °C. The procedures for acquisition of U87MG-$IDH1^{WT}$ and U87MG-$IDH1^{R132}$ mutant cell lines were previously reported by Lazovic et al. [32].

Animal Model

Male NOD-SCID mice (6–8 weeks old) were used for all experiments. Tumor xenografts were generated via surgical implantation employing a stereotactic technique as described previously by Akhtari et al. [33]. All procedures were approved by the University of California, Los Angeles, Institutional Animal Care and Use Committee.

Tumor Xenograft Assay

Sulfamethoxazole (5 mg/mL)/trimethoprim (1 mg/mL) was administered in drinking water for 2 days before and 5 days following intracranial surgery. Animals were anesthetized with isofluorane gas (5%) and placed in a stereotaxic frame. A 2-cm skin incision was made, and the stereotactic apparatus was used to calculate coordinates (2 mm lateral, 0.5 anterior, and 3.3 down from bregma-lambda level). A hole was drilled to allow cell implantation in the striatum. Three groups of four NOD-SCID mice were injected with 10^6 glioma cells as follows: U87MG vector, U87MG-$IDH1^{WT}$, and U87MG-$IDH1^{R132}$ cells. A total of 2.5 μL of the cell line was stereotactically injected, at the rate of 1.0 μL per min.

Neurological signs such as seizures, weakness, unsteady gait, excessive circling behavior, or marked aggression or timidity, along with signs of pain or discomfort, were considered as signs of tumor progression. Once obvious tumor signs were noted in one mouse, all animals in that group underwent MR imaging to evaluate the actual extent of tumor progression.

Contrast Agent

HYNIC-PEG_4-c(GX1) and HYNIC-E-[c(RGDfk)-c(GX1)] peptides purchased from CPC Scientific Inc. (EUA) were synthesized with the chelator 2-hydrazinonicotinamide (HYNIC), and designed in a cyclic conformation, in order to improve binding abilities and excretion. The peptides were covalently conjugated to nonradioactive magnetonanoparticles (MNPs) via a glycerine linker as described previously [33]. Briefly, the plain particles were characterized by transmission electron microscopy (TEM) with energy-dispersive X-ray spectroscopy (EDAX; Philips, Germany), by atomic force microscopy, as well as by the zeta potential (Zetasizer

300HSA, Malvern Instruments, Malvern, UK). The basic experiment data about the characterization of the functionalized magnetic nanoparticles were already published and also included a patent [33–37].

Magnetic Resonance Imaging

MRI studies were performed using a 7-T Bruker system with a custom-built 2.2-cm radiofrequency birdcage coil. Images were acquired at 14 and 21 days following the intracranial injections of glioma cells to correspond to clinically active disease. Before imaging, animals were anesthetized with isoflurane (4% for induction, maintenance with 1.5%). During imaging, respiration was monitored and isoflurane levels were adjusted if frequency was less than 60 or more than 80 breaths per minute. Mice were kept warm with a closed system water heater at 37 °C and circulated using a TP500 water pump (Gaymar Solid State).

Animals were injected (i.v. tail vein) with 100 μL of MNP-HYNIC-PEG_4-c(GX1) or MNP-HYNIC-E-[c(RGDfk)-c(GX1)] contrast (referenced as GX1 or RGD-GX1 to simplify). This corresponds to 3.5 mg Fe/kg, considering the weight of the hydrous iron oxide core of the magnetonanoparticles. Each animal had one baseline (pre-contrast) and five post-contrast MR scans obtained at 15, 30, 60, 90, and 120 min after injection. Control studies were performed through the injection of plain unconjugated magnetonanoparticles.

Transverse relaxation times (T_2) of tumors were measured using a multislice multiecho (MSME) sequence (spin echo, TR/TE = 2000/7.26–101.64 ms, 14 echoes, 78-mm^2 in-plane resolution, and 1-mm slice thickness). Acquisition time was 19 min. Subtraction data were processed offline using ImageJ (National Institutes of Health) and the MRI Analysis Calculator plug-in. T_2-subtraction maps ($\Delta T_2\ (t) = T_{2\ (\text{pre-contrast})} - T_{2\ (t\text{post-contrast})}$) were generated for different time points as to aid in visualization of contrast enhancement.

Animals were euthanized at the conclusion of the studies through anesthesia with pentobarbital (100 mg/kg i.p.) followed by cervical dislocation, according to recommendations of the animal facility veterinarians (need to name the standard).

Histology

Following sacrifice, animals' tumor tissues were excised and fixed by immersion into 4% formalin overnight and then embedded in paraffin. Sections (10 mm thick) were cut, deparaffinized, and stained by standard hematoxylin and eosin (H&E) technique. Immunohistochemistry for CD31 membrane protein (putative ligand for $\alpha v\beta 3$ integrin) was performed using rat anti-mouse-CD31 antibody (DIA-310, Dianova, Germany) to determine if contrast enhancement pattern observed on MR images will match the presence of endothelial cells. Stained sections were matched and compared with T_2 maps to visually inspect if regions with increased numbers of CD31-positive cells corresponded with decreased T_2 values following magnetonanoparticle injections. Also, the iron staining was performed (Iron Stain Kit ab150674, Abcam, Cambridge, UK) to investigate the iron presence from magnetonanoparticles in the tissue.

Statistical Analysis

All data were expressed as mean ± standard deviation (SD). Normal distribution of data was first tested using normality test (Shapiro-Wilk), and then, data sets were analyzed by Student's

t test. Sigma Stat software (Jandel Scientific, San Rafael, CA) was used for analysis. All *p* values less than 0.05 were considered statistically significant.

Results

U87MG-Vector Glioblastoma Shows Enhanced GX1-Magnetonanoparticle Contrast Uptake

Subtraction ΔT_2 maps at different time points of mice bearing U87MG vector tumor injected with MNP-HYNIC-PEG$_4$-c(GX1) and MNP-HYNIC-E-[c(RGDfk)-c(GX1)] are shown in Fig. 1, respectively. Figure. 1a, g represents the T_2-weighted images, with tumor region outline with dotted red line. Figure 1b–f, h–l shows the representative ΔT_2 (t) maps, aimed at visualization of magnetonanoparticle accumulation in time. Significant ($P < 0.05$) decrease in T_2 values compared to normal brain parenchyma was found for all time points. In addition, ΔT_2 values increased in time, indicating additional accumulation of particles, peaking at ~120 min post-injection for both contrasts.

Prior to and following magnetonanoparticle injection, there was similar T_2 distribution within the tumor ROI (Fig. 1m). T_2 values are calculated for same tumor at two different days injected with MNP-GX1 or MNP-RGD-GX1 particles. In both cases, the highest value occurred at 2 h, in which MNP-HYNIC-PEG$_4$-c(GX1) reached 20.2% and MNP-HYNIC-E-[c(RGDfk)-c(GX1)] 18.6%; however, this difference was not significant ($P > 0.05$).

Representative T_2-weighted image and ΔT_2 maps for mice bearing U87MG-IDH1^{WT} tumor injected with MNP-HYNIC-PEG$_4$-c(GX1) and with MNP-HYNIC-E-[c(RGDfk)-c(GX1)] are shown in Fig. 2. Figure 2b–f shows the ΔT_2 maps at different times, correlated with magnetonanoparticle uptake. During the first three points (15, 30, and 60 min), the tumor uptake was lower, subsequently increasing at 90 min and reaching the maximum at 120 min post-injection. Figure 2h–l corresponds to the magnetonanoparticle uptake. At all times, tumor uptake was low.

Changes in T_2 values for U87MG-IDH1^{WT} tumors at different time points are shown in Fig. 2m. Signal reduction is evident, indicating conjugated-MNP tumor uptake soon after contrast injection. With MNP-HYNIC-PEG$_4$-c(GX1), uptake is noticed at 15 min, increasing

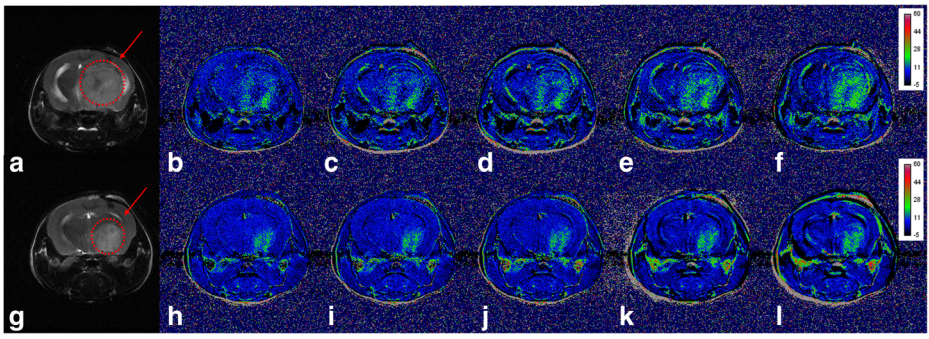

Fig. 1 MR images of U87MG vector xenograft mouse with MNP-HYNIC-PEG$_4$-c(GX1). **a** T_2-weighted image without contrast. Subtraction images at **b** 0–15 min, **c** 0–30 min, **d** 0–1 h, **e** 0–1 h and 30 min, and **f** 0–2 h post-injection, with MNP-HYNIC-E-[c(RGDfk)-c(GX1)]. **g** T_2-weighted baseline image without contrast. Subtraction images at **h** 0–15 min, **i** 0–30 min, **j** 0–1 h, **k** 0–1 h and 30 min, and **l** 0–2 h post-injection

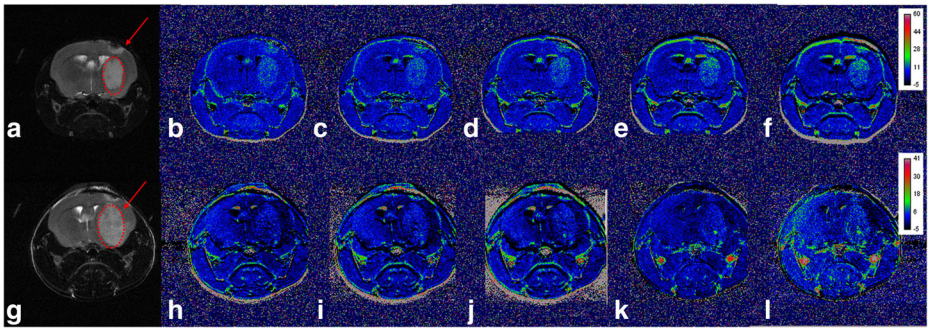

Fig. 2 MR images of U87MG-IDH1^{WT} xenograft mouse with MNP-HYNIC-PEG$_4$-c(GX1). **a** RARE baseline without contrast. Subtraction images at **b** 0–15 min, **c** 0–30 min, **d** 0–1 h, **e** 0–1 h and 30 min, and **f** 0–2 h post-injection, with MNP-HYNIC-E-[c(RGDfk)-c(GX1)]. **g** RARE baseline without contrast. Subtraction images at **h** 0–15 min, **i** 0–30 min, **j** 0–1 h, **k** 0–1 h and 30 min, and **l** 0–2 h post-injection

with time and achieving 14.66% at 2 h post-injection. As visualized in all images, MNP-HYNIC-E-[c(RGDfk)-c(GX1)] uptake was low, not exceeding 3.5% at 2 h post-injection.

T_2-weighted image and ΔT_2 maps of U87MG-IDH1^{R132} xenograft injected with MNP-HYNIC-PEG$_4$-c(GX1) and MNP-HYNIC-E-[c(RGDfk)-c(GX1)] can be appreciated in Fig. 3. Figure 3b–f, g–l shows the ΔT_2 maps at different times, correlated with conjugated-MNP uptake. For both contrasts, at 15 and 30 min, response was mild; however, at 60 min, uptake increased, reaching the highest value at 120 min post-injection.

Figure 3m displays the T_2 quantification values for U87MG-IDH1^{R132} tumor ROI. With both conjugates, increased uptake (signal reduction) was observed with time. MNP-HYNIC-E-[c(RGDfk)-c(GX1)] exhibited somewhat higher reduction, consistent with a more robust binding, reaching 15.84% for RGD-GX1 and 12.39% for GX1. Nevertheless, this difference was not statistically significant ($P > 0.05$).

In Fig. 4, U87MG tumor injected with plain MNP is assessed as a negative control. Figure 4b–f corresponds to subtraction uptake. At all times, tumor uptake was low. Figure 4g shows the ΔT_2 maps for different imaging times. Signal reduction is small, demonstrating a minor uptake in the tumor tissue. There was no statistically significant difference in ΔT_2 values

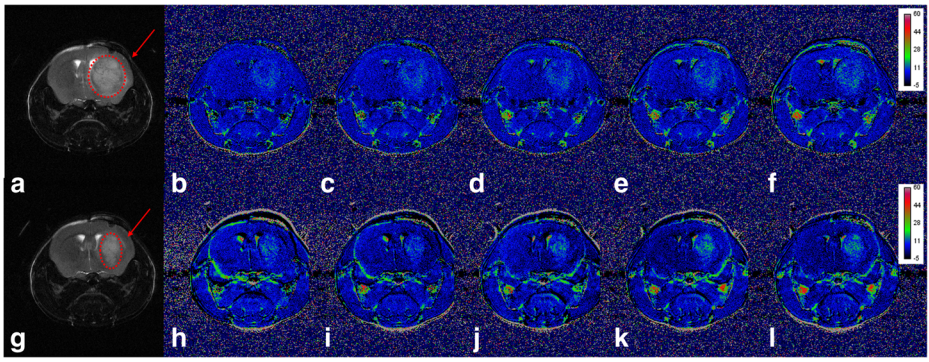

Fig. 3 MR images of U87MG-IDH1^{R132} xenograft mouse with MNP-HYNIC-PEG$_4$-c(GX1). **a** T_2-weighted baseline image without contrast. Subtraction images at **b** 0–15 min, **c** 0–30 min, **d** 0–1 h, **e** 0–1 h and 30 min, and **f** 0–2 h post-injection, with MNP-HYNIC-E-[c(RGDfk)-c(GX1)]. **g** T_2-weighted baseline image without contrast. Subtraction images at **h** 0–15 min, **i** 0–30 min, **j** 0–1 h, **k** 0–1 h and 30 min, and **l** 0–2 h post-injection

between tumor tissue and the normal brain tissue, indicating lack of tumor-specific uptake of plain MNP. Table 1 summarizes the uptake percentage by both conjugated peptides in all the times and cell lines used in the study. This comparison helps the understanding of the results and point to the 2-h time as the better time to visualize the tumors.

MR Signal Changes Observed on ΔT_2 Maps Correlate with CD31 and Iron Staining

Similar to observed highest changes on ΔT_2 maps, it was found that U87MG-vector tumors had the highest density of CD31-positive cells (Fig. 5) and intraluminal iron deposits (Fig. 6). The region with smallest ΔT_2 value in this tumor was found to be necrotic (Fig. 5b, yellow square) with sparse CD31-positive cells. The distribution and number of CD31-positive cells were similar for U87MG-IDH^{R132} and U87MG-IDH^{WT} tumors (Fig. 5d, f–i). The region with low ΔT_2 values (Fig. 5g, red square) in U87MG-IDH1^{WT} tumor was found to have lower number of CD31-positive cells (Fig. 5h) compared to the region with higher ΔT_2 values (red square) and more CD31-positive cells (Fig. 5i). Very sparse CD31 staining was present in the normal brain region (Fig. 5e), consistent with very low ΔT_2 values and reduced magnetonanoparticle uptake. Iron uptake (Fig. 6) confirms the presence of iron deposits in the tissue.

Discussion

The specific binding potential of GX1- and RGD-GX1-conjugated peptides to target glioblastoma multiforme was evaluated. Experimental findings for both MNP-HYNIC-PEG$_4$-c(GX1) and MNP-HYNIC-E-[c(RGDfk)-c(GX1)] were similar for U87MG vector and U87MG-IDH1^{R132} tumor cells, whereas for U87MG-IDH1^{WT}, only MNP-HYNIC-PEG$_4$-c(GX1) achieved successful binding. Small and large molecules are known to have similar peak tumor

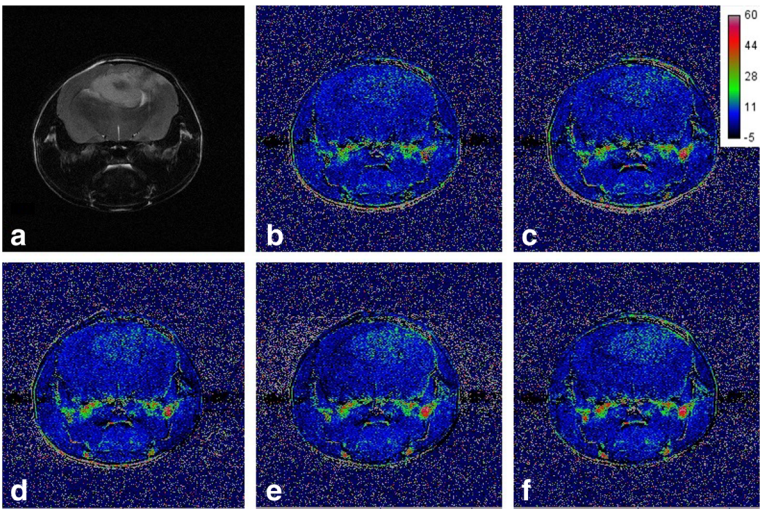

Fig. 4 MR images of U87MG-IDH1^{WT} xenograft mouse. **a** T_2-weighted baseline image without contrast. Subtraction images with plain MNP at **b** 0–30 min, **c** 0–1 h, **d** 0–1 h and 30 min, **e** 0–2 h, and **f** 0–2 h and 30 min post-injection

Table 1 Comparison of the conjugated peptides during the time in the three glioma cell lines tested

Time	Glioma cell line					
	U87MG vector		U87MG-IDH1^{WT}		U87MG-IDH1^{R132}	
	GX1	RGD-GX1	GX1	RGD-GX1	GX1	RGD-GX1
15 min	87.22 ± 10.10%	83.36 ± 5.15%	86.08 ± 5.42%	97.15 ± 7.08%	84.54 ± 7.16%	87.96 ± 5.63%
30 min	86.10 ± 9.29%	82.80 ± 5.00%	86.23 ± 5.42%	95.83 ± 6.59%	84.83 ± 6.55%	89.63 ± 5.63%
60 min	86.03 ± 9.78%	82.78 ± 5.31%	85.09 ± 6.02%	96.48 ± 6.59%	82.79 ± 6.71%	87.38 ± 5.47%
90 min	82.40 ± 8.97%	82.30 ± 4.84%	84.37 ± 5.72%	93.58 ± 6.26%	83.16 ± 6.71%	84.21 ± 4.99%
120 min	79.73 ± 10.11%	81.41 ± 9.05%	85.33 ± 6.02%	96.51 ± 6.26%	84.10 ± 7.32%	84.16 ± 5.47%

GX1 MNP-HYNIC-PEG4-c(GX1), *RGD-GX1* MNP-HYNIC-E-[c(RGDfk)-c(GX1)]

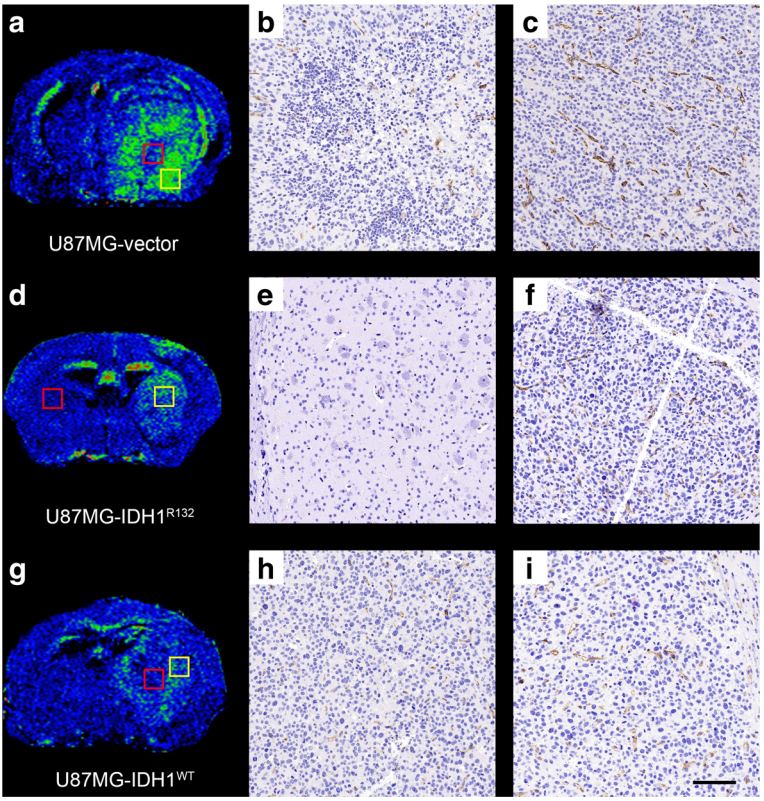

Fig. 5 Immunohistochemistry for CD31 membrane protein. **a** Subtraction MR image at 2 h for U87MG-vector injected mouse. Areas with more contrast enhancement (*red square*) showed many CD31-positive endothelial cells (**c**), while necrotic region (*yellow square*) showed sparse CD31-positive cells (**b**). For mice injected with U87MG-IDH1^{R132} glioma cells, distribution of CD31-positive cells was similar throughout the tumor (**e**, **f**) consistent with similar contrast enhancement observed (*yellow and red squares*). **g** Subtraction MR image for U87MG-IDH1^{WT}-bearing mice. Contrast enhancement matched well with presence of CD31-positive cells (*yellow square*) (**i**), while area void of contrast enhancement showed sparse CD31 staining (*red square*) (**h**). *Scale bar* represents 100 μm

levels, but they differ in time and affinity uptake. Small proteins, such GX1 alone, require high affinity to be retained and are rapidly cleared from the blood and normal tissues, making them suitable for imaging applications. Large molecules require more time to accumulate in the

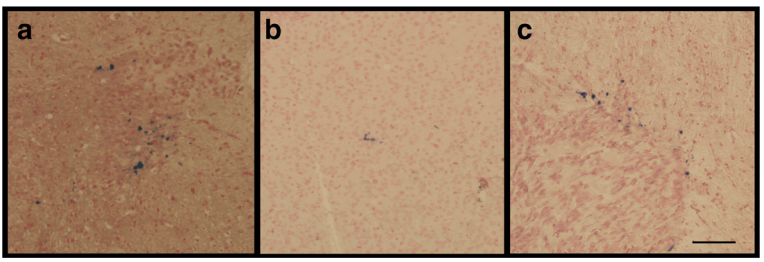

Fig. 6 Iron staining showing the presence of iron deposits in glioma slices from animals' brain. **a** U87MG-vector mouse. **b** U87MG-IDH1^{R132}. **c** U87MG-IDH1^{WT}. *Scale bar* represents 100 μm

tumor, suggesting a possible explanation for RGD-GX1-conjugated lower uptake in U87MG-IDH1^{WT} tumor [38, 39].

Studies such as immunohistochemical staining, ELISA, and immunofluorescence indicate that GX1 might be used as a vascular marker for human cancers [9, 18]. Although the GX1 receptor remains unknown, Hu et al. [22] suggest integrin $\alpha 3\beta 1$ as a possible candidate, on the basis of mass spectrometry tests. Such identification might help to elucidate the mechanism of GX1-mediated anti-angiogenic effects.

The peptides were conjugated with 6-hydrazinonicotinic acid (HYNIC), which is a bifunctional ligand, widely used in the building of molecular imaging agents. It helps to increase stability and accelerate excretion with lower accumulation in the body [40–43]. PEGylation is the most efficient strategy to improve pharmacokinetics due to the ability of creating steric hindrance. As a consequence, significant inhibition of protein adsorption, less recognition by the phagocyte system, increase in the size of the molecules, reduced glomerular filtration rate, and stronger tumor uptake occur partly also due to the branched chemical structure [44, 45]. These are preferable features in the design of new molecules. This insertion was not possible in the RGD-GX1 molecule precisely because of a steric barrier. The use of PEG_4 does not affect the binding affinity at the target tissues, as already well demonstrated in the literature [46, 47]. Only the active sites to the target tissues were relevant, and these were well preserved. The other manipulations in the molecules were purely technical and devoid of interference with the active sites.

IDH1^{R132} mutation was found to contribute to better prognosis in patients diagnosed with glioblastoma [7]; for this reason, we decided to evaluate glioma cell lines harboring this specific mutation, as well the wild-type mutation, to investigate if our conjugates would also detect all this groups as a good advantage for a future glioma detector probe. Based on our results, it appears that U87MG-IDH1^{R132} tumors had reduced density of CD31 staining compared to U87MG-vector tumors. Therefore, less rapid tumor proliferation might be expected due to reduced potential for angiogenesis. Mutant IDH1 lesions could also result in increased reactive oxygen species and heightened oxidative response. Deranged tumor growth linked to sustained activation of cell-cycle inhibitor might follow, inducing apoptosis and necrosis [48–51]. Indeed, in our findings, the IDH1 tumors present necrotic areas, and U87MG-vector tumors show higher uptakes due to higher vascularization, which are in accordance with literature.

The option for an orthotopic glioma model, though technically cumbersome, has advantages compared to a heterotransplantation model, as it more closely mimics the brain tumor environment [52]. The blood–brain barrier (BBB) hinders the access of most chemical compounds to the brain tissues, notably large nonlipophilic molecules. Whereby the target of our magnetic nanoparticles conjugated with peptides is the new vasculature present in tumors, they do not need to cross the BBB to provide good imaging. In such circumstances, the successful localization in tumor area bodes well for the clinical future of the tested peptides.

Studies in nanotechnology have led to the development and synthesis of various nonradioactive MNPs, which change the magnetic environment of the surrounding protons and alter T_1 and/or T_2 signal in a concentration-dependent manner, once introduced in body tissues. Some of the advantages are that these particles cross the blood–brain barrier and localize to tumor tissues [34, 53–56]. All these features contribute for the wide application of nanoparticles in the medical field. Successful cancer management depends on accurate diagnostics along with specific treatment protocols. Innovative technologies based on nanotechnology has been used to improve several aspects of health care approaches, which provide earlier detection of tumors, besides the patient follow-up, by imaging and drug delivery techniques [57, 58].

Magnetic particles have found many applications in many biomedical fields. Very recently, Zhou et al. [59] synthesized a multifunctional peptide-fluorescent-magnetic nanocomposite for potential application to cancer diagnoses. Data from in vitro cytotoxicity assay and in vivo fluorescent imaging and MRI showed that the nanocomposites could recognize the lung cancer stem cells. Rosenberger et al. [60] developed magnetic biodegradable nanoparticles using recombinant human serum albumin (rHSA) and incorporated iron oxide (maghemite, γ-Fe_2O_3) nanoparticles with success for diagnostic of pancreatic cancer. Akhtari et al. [34] attached the same magnetonanoparticles used in this study to nonradioactive alpha methyl tryptophan (AMT) to accurately localize epileptogenic cerebral regions.

Although only very recently GX1 peptide has been studied in conjugation with a paramagnetic contrast during MR imaging [61], there are some studies with RGD. Liu et al. [62] evaluated a novel $\alpha v\beta 3$ integrin-targeted MRI contrast agent, RGD-ultrasmall superparamagnetic iron oxide particles (USPIO), which can specifically depict the angiogenic profile of lung cancer using a 4.7-T MR scanner. Zhang et al. [63] also studied RGD conjugated to USPIO. They were able to distinguish tumors differing in the degree of $\alpha v\beta 3$ integrin expression and angiogenesis profile, even when using a standard clinical 1.5-T MRI scanner. Park et al. [64] described a Gd-DOTA-RGD conjugate for MRI, as a potential tumor targeting agent for hepatocellular carcinoma.

More recently, magnetic nanoclusters coated with ruthenium (II) complexes doped with silica attached to the RGD peptide were used for specific targeting in human breast cancer to image tumors through magnetic resonance imaging [65]. The results were favorable to RGD-FMNPs, with decreased T_2 values in tumor regions, demonstrating its potential targeting of a very wide range of cancer types. Also, Yang et al. [66] developed an ultrasmall iron oxide nanoparticles conjugated with RGD for targeted MR imaging of C6 glioma cells through a dendrimer-mediated approach. The conjugated molecule obtained good hemocompatibility and biocompatibility and has high affinity for glioma cells overexpressing $\alpha v\beta 3$ receptors.

Current images show a heterogeneous tumor morphology similar to CD31 staining pattern and distribution of new vessels, which tends to be somewhat irregular. Such difficulty notwithstanding, the development of MRI contrast agents which cross the BBB and accumulate in the tumor could improve accuracy of detecting tumor burden, including small tumors and those infiltrating normal adjacent brain. The novelty of this study was to render two tumor-specific peptides visible on MRI and assess their utility in producing contrast enhancement in tumors compared to plain MNPs.

The ability of GX1-based peptides conjugated to MNP to identify intracranial tumors would have several advantages. Most importantly, the prevalence of MRI technology worldwide, the lack of need for additional specialized equipment, and the relatively long shelf life of these contrast agents, which are nonradioactive, will increase accessibility for imaging compared to PET or SPECT techniques. Additional advantages are the excellent anatomical resolution of MRI compared with nuclear modalities and that MRI studies with these contrast agents can be safely repeated when indicated.

Conclusions

This study supports the potential application of nonradioactive GX1-based peptides conjugated with magnetonanoparticles to improve visualization of glioma tumor on MRI. In this sense, it should be considered in future studies, aiming to evaluate degree of angiogenesis in gliomas as well as other tumor models.

Acknowledgements The authors are grateful for a post-graduate grant by Fundação de Amparo a Pesquisa do Estado de São Paulo, Brazil (FAPESP 2011/12405-0). We thank preclinical imaging and histology unit of Vienna Biocenter Core Facilities (VBCF) for their help with this manuscript.

Compliance with Ethical Standards

Funding Funding was provided by Fundação de Amparo a Pesquisa do Estado de São Paulo, Brazil (FAPESP 2011/12405-0).

Ethical Approval All applicable international, national, and/or institutional guidelines for the care and use of animals were followed. All procedures were approved by the University of California, Los Angeles, Institutional Animal Care and Use Committee.

Conflict of Interest The authors declare that they have no conflict of interest.

References

1. Ostrom, Q. T., Gittleman, H., Liao, P., Rouse, C., Chen, Y., Dowling, J., Wolinsky, Y., Kruchko, C., & Barnholtz-Sloan, J. (2014). CBTRUS statistical report: primary brain and central nervous system tumors diagnosed in the United States in 2007–2011. *Neuro-Oncology, 16*(Suppl 4), iv1–i63.
2. Bello, L., Giussani, C., Carrabba, G., Pluderi, M., Costa, F., & Bikfalvi, A. (2004). Angiogenesis and invasion in gliomas. *Cancer Treatment and Research, 117*, 263–284.
3. Skobe, M., Rockwel, L. P., Goldstein, N., Vosseler, S., & Fusenig, N. E. (1997). Halting angiogenesis suppresses carcinoma cell invasion. *Nature Med., 3*, 1222–1227.
4. Parsons, D. W., Jones, S., Zhang, X., Lin, J. C., Leary, R. J., Angenendt, P., Mankoo, P., Carter, H., Siu, I. M., Gallia, G. L., Olivi, A., McLendon, R., Rasheed, B. A., Keir, S., Nikolskaya, T., Nikolsky, Y., Busam, D. A., Tekleab, H., Diaz Jr., L. A., Hartigan, J., Smith, D. R., Strausberg, R. L., Marie, S. K., Shinjo, S. M., Yan, H., Riggins, G. J., Bigner, D. D., Karchin, R., Papadopoulos, N., Parmigiani, G., Vogelstein, B., Velculescu, V. E., & Kinzler, K. W. (2008). An integrated genomic analysis of human glioblastoma multiforme. *Science, 321*(5897), 1807–1812.
5. Yan, H., Parsons, D. W., Jin, G., McLendon, R., Rasheed, B. A., Yuan, W., Kos, I., Batinic-Haberle, I., Jones, S., Riggins, G. J., Friedman, H., Friedman, A., Reardon, D., Herndon, J., Kinzler, K. W., Velculescu, V. E., Vogelstein, B., & Bigner, D. D. (2009). IDH1 and IDH2 mutations in gliomas. *The New England Journal of Medicine, 360*(8), 765–773.
6. Xu, X., Zhao, J., Xu, Z., Peng, B., Huang, Q., Arnold, E., & Ding, J. (2004). Structures of human cytosolic NADP-dependent isocitrate dehydrogenase reveal a novel self-regulatory mechanism of activity. *The Journal of Biological Chemistry, 279*(32), 33946–33957.
7. Nobusawa, S., Watanabe, T., Kleihues, P., & Ohgaki, H. (2009). IDH1 mutations as molecular signature and predictive factor of secondary glioblastomas. *Clinical Cancer Research, 15*(19), 6002–6007.
8. Smith, J. W., & Cheresh, D. A. (1988). The arg-gly-asp binding domain of the vitronectin receptor: photoaffinity cross-linking implicates amino acid residues 61–203 of the ß subunit. *The Journal of Biological Chemistry, 263*, 18726–18731.
9. Zhi, M., Wu, K. C., Dong, L., Hao, Z. M., Deng, T. Z., Hong, L., Liang, S. H., Zhao, P. T., Qiao, T. D., Wang, Y., Xu, X., & Fan, D. M. (2004). Characterization of a specific phage-displayed peptide binding to vasculature of human gastric cancer. *Cancer Biology & Therapy, 3*, 1232–1235.
10. Dijkgraaf, I., Kruijtzer, A. W., Liu, S., Soede, A. C., Oyen, W. J. G., Corstens, F. H. M., Liskamp, R. M. J., & Boerman, O. C. (2007). Improved targeting of the avb3 integrin by multimerisation of RGD peptides. *European Journal of Nuclear Medicine and Molecular Imaging, 34*(2), 267–273.
11. Liu, S., Kim, Y. S., Hsieh, W. Y., & Sreerama, S. G. (2008). Coligant effect on the solution stability, biodistribution and metabolism of the 99mTc-labeled cyclic RGDfK tetramer. *Nuclear Medicine and Biology, 35*, 111–121.
12. Moncelet, D., Bouchaud, V., Mellet, P., Miraux, S., Franconi, J. M., & Voisin, P. (2013). Cellular density effect on RGD ligand internalization in glioblastoma for MRI application. *PloS One, 8*(12), e82777.
13. Schottelius, M., & Wester, H. J. (2009). Molecular imaging targeted receptor. *Methods, 48*, 161–177.

14. Zhang, X., Xiong, Z., Wu, Y., Cai, W., Tseng, J. R., Gambhir, S. S., & Chen, X. (2006). Quantitative PET imaging of tumor integrin alphavbeta3 expression with 18F-FRGD2. *Journal of Nuclear Medicine, 47*(1), 113–121.
15. Desgrosellier, J. S., & Cheresh, D. A. (2010). Integrins in cancer: biological implications and therapeutic opportunities. *Nature Reviews. Cancer, 10*, 9–22.
16. Guo, W., & Giancotti, F. G. (2004). Integrin signalling during tumour progression. *Nature Reviews. Molecular Cell Biology, 5*, 816–826.
17. Hynes, R. O. (1992). Integrins: versatility, modulation, and signaling in cell adhesión. *Cell, 69*(1), 11–25.
18. Jin, Z. H., Furukawa, T., Waki, A., Akaji, K., Coll, J. L., Saga, T., & Fujibayashi, Y. (2010). Effect of multimerization of a linear arg-gly-asp peptide on integrin binding affinity and specificity. *Biological & Pharmaceutical Bulletin, 33*(3), 370–378.
19. Wu, H., Chen, H., Pan, D., Ma, Y., Liang, S., Wan, Y., & Fang, Y. (2014). Imaging integrin αvβ 3 and NRP-1 positive gliomas with a novel fluorine-18 labeled RGD-ATWLPPR heterodimeric peptide probe. *Molecular Imaging and Biology, 16*(6), 781–792.
20. Chen, B., Cao, S., Zhang, Y., Wang, X., Liu, J., Hui, X., Wan, Y., Du, W., Wang, L., Wu, K., & Fan, D. (2009). A novel peptide (GX1) homing to gastric cancer vasculature inhibits angiogenesis and cooperates with TNF alpha in anti-tumor therapy. *BMC Cell Biology, 10*, 63.
21. Chen, K., Sun, X., Niu, G., Ma, Y., Yap, L., Hui, X., Wu, K., Fan, D., Conti, P. S., & Chen, X. (2012). Evaluation of 64Cu labeled GX1: a phage display peptide probe for PET imaging of tumor vasculature. *Molecular Imaging and Biology, 14*(1), 96–105.
22. Hu, H., Yin, J., Wang, M., Liang, C., Song, H., Wang, J., Nie, Y., & Liang, J. (2014). GX1 targeting delivery of rmhTNFα evaluated using multimodality imaging. *International Journal of Pharmaceutics, 461*(1–2), 181–191.
23. Hui, X., Han, Y., Liang, S., Liu, Z., Liu, J., Hong, L., Zhao, L., He, L., Cao, S., Chen, B., Yan, K., Jin, B., Chai, N., Wang, J., Wu, K., & Fan, D. (2008). Specific targeting of the vasculature of gastric cancer by a new tumor-homing peptide CGNSNPKSC. *Journal of Controlled Release, 131*, 86–93.
24. Xin, J., Zhang, X., Liang, J., Xia, L., Yin, J., Nie, Y., Wu, K., & Tian, J. (2013). In vivo gastric cancer targeting and imaging using novel symmetric cyanine dye-conjugated GX1 peptide probes. *Bioconjugate Chemistry, 24*(7), 1134–1143.
25. Li, Z. B., Wu, Z., Chen, K., Ryu, E. K., & Chen, X. (2008). 18F-labeled BBN-RGD heterodimer for prostate cancer imaging. *Journal of Nuclear Medicine, 49*, 453–461.
26. Liu, Z., Yan, Y., Chin, F. T., Wang, F., & Chen, X. (2009). Dual integrin and gastrin-releasing peptide receptor targeted tumor imaging using 18F-labeled PEGylated RGD-bombesin heterodimer 18F-FB-PEG3-Glu-RGD-BBN. *Journal of Medicinal Chemistry, 52*(2), 425–432.
27. Yang, J., Guo, H., Galazzi, F., Berwick, M., Padilla, R. S., & Miao, Y. (2009). Evaluation of a novel arg-gly-asp-conjugated r-melanocyte stimulating hormone hybrid peptide for potential melanoma therapy. *Bioconjugate Chemistry, 20*, 1634–1642.
28. Yang, J., Guo, H., & Miao, Y. (2010). Technetium-99m-labeled arg-gly-asp-conjugated alpha-melanocyte stimulating hormone hybrid peptides for human melanoma imaging. *Nuclear Medicine and Biology, 37*(8), 873–883.
29. Liu, Z., & Wang, F. (2010). Dual-targeted molecular probes for cancer imaging. *Current Pharmaceutical Biotechnology, 11*, 610–619.
30. Oliveira, E. A., & Faintuch, B. L. (2015). Radiolabeling and biological evaluation of the GX1 and RGD-GX1 peptide sequence for angiogenesis targeting. *Nuclear Medicine and Biology, 42*(2), 123–130.
31. Oliveira, E. A., Faintuch, B. L., Targino, R. C., Moro, A. M., Martinez, R. C., Pagano, R. L., Fonoff, E. T., Carneiro, C. G., Garcez, A. T., Faria, D. P., & Buchpiguel, C. A. (2016). Evaluation of GX1 and RGD-GX1 peptides as new radiotracers for angiogenesis evaluation in experimental glioma models. *Amino Acids, 48*(3), 821–831.
32. Lazovic, J., Soto, H., Piccioni, D., Lou, J. R., Li, S., Mirsadraei, L., Yong, W., Prins, R., Liau, L. M., Ellingson, B. M., Cloughesy, T. F., Lai, A., & Pope, W. B. (2012). Detection of 2-hydroxyglutaric acid in vivo by proton magnetic resonance spectroscopy in U87 glioma cells overexpressing isocitrate dehydrogenase-1 mutation. *Neuro-Oncology, 14*(12), 1465–1472.
33. Akhtari, M., Bragin, A., Moats, R., Frew, A., & Mandelkern, M. (2012). Functionalized magnetonanoparticles in imaging brain neuronal activity using MRI. *Brain Topography, 25*(4), 374–388.
34. Akhtari, M., Bragin, A., Cohen, M., Moats, R., Brenker, F., Lynch, M. D., Vinters, H. V., & Engel Jr., J. (2008). Functionalized magnetonanoparticles for MRI diagnosis and localization in epilepsy. *Epilepsia, 49*, 1419–1430.
35. Akhtari, M., Pope, W., Mathern, G., Moats, R., Frew, A., & Mandelkern, M. (2013). Functionalized magnetonanoparticles in visualization of intracranial tumors on MRI. *Molecular Imaging and Biology, 15*(3), 299–306.

36. Akhtari, M., & Engel, J. (2006). Patents PCT/US06/10334. EU06739214.2.
37. Akhtari, M., & Engel, J. (2009). Pat # WO 2009/123734 A1.
38. Goldenberg, D. M., Sharkey, R. M., Paganelli, G., Barbet, J., & Chatal, J. F. (2006). Antibody pretargeting advances cancer radioimmunodetection and radioimmunotherapy. *Journal of Clinical Oncology, 24*, 823–834.
39. Orlova, A., Magnusson, M., Eriksson, T. L., Nilsson, M., Larsson, B., Höidén-Guthenberg, I., Widström, C., Carlsson, J., Tolmachev, V., Ståhl, S., & Nilsson, F. Y. (2006). Tumor imaging using a picomolar affinity HER2 binding affibody molecule. *Cancer Research, 66*, 4339–4348.
40. Decristoforo, C., Faintuch-Linkowski, B., Rey, A., von Guggenberg, E., Rupprich, M., Hernandez-Gonzales, I., Rodrigo, T., & Haubner, R. (2006). [99mTc]HYNIC-RGD for imaging integrin alphavbeta3 expression. *Nuclear Medicine and Biology, 33*, 945–952.
41. Decristoforo, C., Santos, I., Pietzsch, H. J., Kuenstler, J. U., Duatti, A., Smith, C. J., Rey, A., Alberto, R., Von Guggenberg, E., & Haubner, R. (2007). Comparison of in vitro and in vivo properties of [99mTc]cRGD peptides labeled using different novel Tc-cores. *The Quarterly Journal Nuclear Medicine and Molecular Imaging, 51*, 33–41.
42. Janssen, M. L., Oyen, W. J., Dijkgraaf, I., Massuger, L. F., Frielink, C., Edwards, D. S., Rajopadhye, M., Boonstra, H., Corstens, F. H., & Boerman, O. C. (2002). Tumor targeting with radiolabeled alpha(v)beta(3) integrin binding peptides in a nude mouse model. *Cancer Research, 62*, 6146–6151.
43. Su, Z. F., He, J., Rusckowski, M., & Hnatowich, D. J. (2003). In vitro cell studies of technetium-99m labeled RGD-HYNIC peptide, a comparison of tricine and EDDA as co-ligands. *Nuclear Medicine and Biology, 30*, 141–149.
44. Denardo, S. J., Yao, Z., Lam, K. M., Song, A., Burker, P. A., Merick, G. R., Lamborn, K. R., O'Donnell, R. T., & Denardo, G. L. (2003). Effect of molecular size of pegylated peptide on the pharmacokinetics and tumor targeting in lymphoma-bearing mice. *Clinical Cancer Research, 1*(9), 38545–38645.
45. Vonarbourg, A., Passirani, C., Saulnier, P., & Benoit, J. P. (2006). Parameters influencing the stealthiness of colloidal drug delivery systems. *Biomaterials, 27*(24), 4356–4373.
46. Däpp, S., García Garayoa, E., Maes, V., Brans, L., Tourwé, D. A., Müller, C., & Schibli, R. (2011). PEGylation of (99m)Tc-labeled bombesin analogues improves their pharmacokinetic properties. *Nuclear Medicine and Biology, 38*(7), 997–1009.
47. Mier, W., Krämer, S., Zitzmann, S., Altmann, A., Leotta, K., Schierbaum, U., Schnölzer, M., Eisenhut, M., & Haberkorn, U. (2013). PEGylation enables the specific tumor accumulation of a peptide identified by phage display. *Organic & Biomolecular Chemistry, 11*(16), 2706–2711.
48. Hampton, M. B., & Orrenius, S. (1997). Dual regulation of caspase activity by hydrogen peroxide: implications for apoptosis. *FEBS Letters, 414*(3), 552–556.
49. Li, S., Chou, A. P., Chen, W., Chen, R., Deng, Y., Phillips, H. S., Selfridge, J., Zurayk, M., Lou, J. J., Everson, R. G., Wu, K. C., Faull, K. F., Cloughesy, T., Liau, L. M., & Lai, A. (2013). Overexpression of isocitrate dehydrogenase mutant proteins renders glioma cells more sensitive to radiation. *Neuro-Oncology, 15*(1), 57–68.
50. Ramsey, M. R., & Sharpless, N. E. (2006). ROS as a tumour suppressor? *Nature Cell Biology, 8*(11), 1213–1215.
51. Takahashi, A., Ohtani, N., Yamakoshi, K., Iida, S., Tahara, H., Nakayama, K., Nakayama, K. I., Ide, T., Saya, H., & Hara, E. (2006). Mitogenic signalling and the p16INK4a-Rb pathway cooperate to enforce irreversible cellular senescence. *Nature Cell Biology, 8*(11), 1291–1297.
52. Fei, X. F., Zhang, Q. B., Dong, J., Diao, Y., Wang, Z. M., Li, R. J., Wu, Z. C., Wang, A. D., Lan, Q., Zhang, S. M., & Huang, Q. (2010). Development of clinically relevant orthotopic xenograft mouse model of metastatic lung cancer and glioblastoma through surgical tumor tissues injection with trocar. *Journal of Experimental & Clinical Cancer Research, 29*, 84.
53. Islam, T., & Harisinghani, M. G. (2009). Overview of nanoparticle use in cancer imaging. *Cancer Biomarkers, 5*, 61–67.
54. Molday, H. S. (1984). US Pat 2,452,773.
55. Muldoon, L. L., Sandor, M., Pinkston, K. E., & Neuwelt, E. A. (2005). Imaging, distribution, and toxicity of superparamagnetic iron oxide magnetic resonance nanoparticles in the rat brain and intracerebral tumor. *Neurosurgery, 57*, 785–796.
56. Pope, W. B., Prins, R. M., Albert Thomas, M., Nagarajan, R., Yen, K. E., Bittinger, M. A., Salamon, N., Chou, A. P., Yong, W. H., Soto, H., Wilson, N., Driggers, E., Jang, H. G., Su, S. M., Schenkein, D. P., Lai, A., Cloughesy, T. F., Kornblum, H. I., Wu, H., Fantin, V. R., & Liau, L. M. (2012). Non-invasive detection of 2-hydroxyglutarate and other metabolites in IDH1 mutant glioma patients using magnetic resonance spectroscopy. *Journal of Neuro-Oncology, 107*(1), 197–205.

57. Chakraborty, M., Jain, S., & Rani, V. (2011). Nanotechnology: emerging tool for diagnostics and therapeutics. *Applied Biochemistry and Biotechnology, 165*(5–6), 1178–1187. doi:10.1007/s12010-011-9336-6 Review.
58. Fernandez-Fernandez, A., Manchanda, R., & McGoron, A. J. (2011). Theranostic applications of nanomaterials in cancer: drug delivery, image-guided therapy, and multifunctional platforms. *Applied Biochemistry and Biotechnology, 165*(7–8), 1628–1651.
59. Zhou, X., Chen, L., Wang, A., Ma, Y., Zhang, H., & Zhu, Y. (2015). Multifunctional fluorescent magnetic nanoparticles for lung cancer stem cells research. *Colloids and Surfaces. B, Biointerfaces, 20*(134), 431–439.
60. Rosenberger, I., Strauss, A., Dobiasch, S., Weis, C., Szanyi, S., Gil-Iceta, L., Alonso, E., González Esparza, M., Gómez-Vallejo, V., Szczupak, B., Plaza-García, S., Mirzaei, S., Israel, L. L., Bianchessi, S., Scanziani, E., Lellouche, J. P., Knoll, P., Werner, J., Felix, K., Grenacher, L., Reese, T., Kreuter, J., & Jiménez-González, M. (2015). Targeted diagnostic magnetic nanoparticles for medical imaging of pancreatic cancer. *Journal of Controlled Release, 17*(214), 76–84.
61. Yan, X., Song, X., Wang, Z. (2016). Construction of specific magnetic resonance imaging/optical dual-modality molecular probe used for imaging angiogenesis of gastric cancer. *Artif Cells Nanomed Biotechnol.* 1–5.
62. Liu, C., Liu, D. B., Long, G. X., Wang, J. F., Mei, Q., Hu, G. Y., Qiu, H., & Hu, G. Q. (2013). Specific targeting of angiogenesis in lung cancer with RGD-conjugated ultrasmall superparamagnetic iron oxide particles using a 4.7 T magnetic resonance scanner. *Chinese Medical Journal, 126*(12), 2242–2247.
63. Zhang, C., Jugold, M., Woenne, E. C., Lammers, T., Morgenstern, B., Mueller, M. M., Zentgraf, H., Bock, M., Eisenhut, M., Semmler, W., & Kiessling, F. (2007). Specific targeting of tumor angiogenesis by RGD-conjugated ultrasmall superparamagnetic iron oxide particles using a clinical 1.5-T magnetic resonance scanner. *Cancer Research, 67*, 1555–1562.
64. Park, J. A., Lee, J. J., Jung, J. C., Yu, D. Y., Oh, C., Ha, S., Kim, T. J., & Chang, Y. (2008). Gd-DOTA conjugate of RGD as a potential tumor-targeting MRI contrast agent. *Chembiochem, 9*, 2811–2813.
65. Sun, J., Teng, Z. G., Tian, Y., Wang, J. D., Guo, Y., Kim, D. H., Larson, A. C., & Lu, G. M. (2014). Targeted fluorescent magnetic nanoparticles for imaging of human breast cancer. *International Journal of Clinical and Experimental Medicine, 7*(12), 4747–4758.
66. Yang, J., Luo, Y., Xu, Y., Li, J., Zhang, Z., Wang, H., Shen, M., Shi, X., & Zhang, G. (2015). Conjugation of iron oxide nanoparticles with RGD-modified dendrimers for targeted tumor MR imaging. *ACS Applied Materials & Interfaces, 7*(9), 5420–5428.